# On studying the interaction between different stent models and rabbit tracheal tissue: numerical, endoscopic and histological comparison

J. Chaure[a], C. Serrano[c], R. Fernández-Parra[c,e], E. Peña[a,b], F. Lostalé[c], M.A. De Gregorio[b,c], M.A. Martínez[a,b], M. Malvè[a,b,d]

[a] *Aragón Institute of Engineering Research. University of Zaragoza, C/María de Luna s/n, E-50018 Zaragoza, Spain.*

[b] *CIBER-BBN. Centro de Investigación en Red en Bioingeniería, Biomateriales y Nanomedicina, C/Poeta Mariano Esquillor s/n, E-50018 Zaragoza, Spain.*

[c] *Grupo de Investigación Técnicas de Mínima Invasión (GITMI), Faculty of Veterinary, Universidad de Zaragoza, C/Miguel Servet 177, E-50013 Zaragoza, Spain.*

[d] *Universidad Pública de Navarra. Departamento de Ingeniería Mecánica, Energética y de Materiales, Campus Arrosadía, E-31006 Pamplona, Spain.*

[e] *Ecole Nationale Vétérinaire d'Alfort, 7 Avenue du Général de Gaulle, F-94704 Maisons-Alfort, France.*

Submitted to Annals of Biomedical Engineering

Abbreviated title: Interaction between different stent types and tracheal tissue

**Corresponding author**:

Estafanía Peña, PhD

Aragón Institute of Engineering Research. University of Zaragoza.

C/María de Luna s/n, E-50018 Zaragoza, Spain.

Phone: (+34) 876 55 5233

Fax: (+34) 976 76 25 78

E-mail: `fany@unizar.es`

**Abstract**

Stenting technique is employed worldwide for treating atherosclerotic vessel and tracheal stenosis. Both diseases can be treated by means of metallic stents which present advantages but are affected by the main problem of restenosis of the stented area. In this study we have built a rabbit trachea numerical model and we have analyzed it before and after insertion and opening of two types of commercial stent: a Zilver® Flex$^{TM}$ Stent and a WallStent$^{TM}$. In experimental parallel work, two types of stent were implanted in 30 New Zealand rabbits divided in two groups of 10 animals corresponding to each stent type and a third group made up of 10 animals without stent. The tracheal wall response was assessed by means of computerized tomography by endoscopy, macroscopic findings and histopathological study 90 days after stent deployment. Three idealized trachea models, one model for each group, were created in order to perform the computational study. **The animal model was used to validate the numerical findings and to attempt to find qualitative correlations between numerical and experimental results. Experimental findings such as inflammation, granuloma and abnormal tissue growth, assessed from histomorphometric analyses were compared with derived numerical parameters such as wall shear stress (WSS) and maximum principal stress**. The direct comparison of these parameters and the biological response supports the hypothesis that WSS and tensile stresses may lead to a greater tracheal epithelium response within the stented region, with the latter seeming to have the dominant role. This study may be helpful for improving stent design and demonstrates the feasibility offered by in-silico investigated tracheal structural and fluid dynamics.

Keywords: Trachea, Nitinol, ZilverFlex$^{TM}$ stent, Wallstent$^{TM}$, fluid-structure interaction, finite element method.

# 1 Introduction

Although in recent years the treatment of tracheal stenosis has been improved by means of tracheobronchial stenting technique, acute inflammation and fibrosis of the tracheal wall [1], in-stent restenosis (ISR) [2,1], trachea obstruction and stent migration [3,4] resulted in a need for further clinical intervention in the stented lesion [2]. The restenosis in airways will occur because of ingrowth of the tumor, granulation **and abnormal tissue growth**. In particular, Fernandez et al. [1] indicate a rate of ISR of $5-20\%$ after stenting surgery. **Dumon [3] found granulation in** $15\%$ **of treated cases, and other associated post-surgery complications such as mucous obstruction in** $3\%$ **of cases, after silicone stent insertion. The reported migration incidence was less than** $20\%$**.** For metallic stents, Fruchter et al. [4] found that granulation and stent obstruction developed in $25\%$ of treated cases while Dasgupta et al. [5] found granulomas and bronchitis as a complication and no migration or mucus plugging was encountered.

Stenting technique is only advisable as a last resort when no other treatment option is available. Many types of stents are commercially available **for the respiratory tract**. The most commonly used, in the case of malign pathologies, are silicone prosthesis and silicone-covered metallic stent, as they prevent restenosis [6]. The most well-known silicone stent is the Dumon stent [3]. Among metallic stents it is important to mention the Gianturco stent which is a self-expanding stent made of stainless steel wire in a zigzag configuration, the Palmaz stent, a balloon-expandable stainless steel tube with laser-etched slot, the Wallstent$^{TM}$, composed of $20-24$ cobalt or stainless steel alloy filaments, with tubular braid configuration and the nitinol memory shape Ultraflex and the Zilver® Flex$^{TM}$ stent [6]. **The Palmaz and Gianturco stents among the cited devices are recently no longer used for the cardiovascular field even they are still used in the experimental studies involving animals [6,7].** Other stent types are the Y-shape hybrid stents, made of combined materials such as silicone and metal, and bioabsorbable stent currently used in animal studies, made of poly-Lactic acid, constructed in a spiral or tubular fashion [6]. Inflammation, migration and obstruction have been reported as the most frequent post-surgery complications [6,3] for silicone prosthesis. On the other hand, recently, implantation of bare metallic stents has also been considered as an efficient way to reestablish the tracheal lumen in the case

of stenosis[8,9]. These devices are normally made of self-expandable biocompatible material[10,2,11].

The application of self expandable metallic stents is generally indicated for malign pathologies[12,13,14,15]. These devices can easily be inserted by flexible bronchoscopy and possess a good radial force which provides a reduction of the migration risk with respect to silicone prosthesis. In addition, the associated re-epithelialization process reduces mucous plugging[2,15,1]. The principal disadvantage of a self-expandable metallic stent is the high risk of restenosis due to cellular proliferation. For this reason, in recent years, bare metallic stents in airways are being replaced more and more by silicone-coated metallic stents. Also, in the cardiovascular field, metallic stent has been covered with pharmaceutical agents[16,17]. Drug eluting stents (DES) have been shown to avoid or reduce the response of the wall to stent struts[18] but their use is still controversial. The reaction of the tracheal wall to the stent can be described as a wound healing response consisting of different phases such as inflammation, cellular proliferation, and tissue remodeling[6,3]. Excessive cellular proliferation leads to the formation of an extensive tissue growth within the stented region for some patients. Abnormal tissue growth has been linked to both non-physiological stresses and wall shear stress applied to the tracheal wall[19,20] as performed in the cardiovascular field where modification of the fluid dynamic environment within the artery has often been correlated with in stent restenosis ISR[21,22,23,24]. Suppression of the response to stent implantation using pharmaceutical agents has demonstrated improvements in treatment, as demonstrated with DES[16,17]. Nevertheless, the understanding of the relationship between the biomechanics modifications which take place after stent deployment and the resulting response of the biological tissue need further improvements such the design of new prosthesis which overcome existing stent design failures and/or development of novel approaches, such as bioresorbable stents[25]. While the complexity of computational studies continues to increase, the relative roles of solid and fluid mechanics in the stenting technique is still in question[23,24,19,20]. While metallic stents are extensively described in literature for cardiovascular applications from a mechanics and fluid dynamics perspective[21,22,23], these devices have not yet been analyzed in the respiratory system. Previous studies have also compared endoscopy images with patient specific trachea geometries and expanded stent models in order to gain qualitative informations about the role of mechanical stresses and fluid dynamic contributions[26,27,20]

but the correlation between the geometry of the stent and the local effects of these stimuli acting on the wall was not carried out. In cases where this data is available, characterization of local stimuli arising from solid and fluid mechanics may help to improve knowledge of the relative importance of these stimuli. Although metallic stents have been studied in the human tracheobronchial tree[4,28,29], there are only a few works which analyze their interaction with the tracheobronchial mucosa. This analysis was performed mainly for the Palmaz stent in rabbits[7], lambs[30] and pigs[31], and for Gianturco stent in dogs[32,33]. Animal models for stenting technique are now crucial in order to have an overview *in vivo* of the associated consequences such as injuries and/or biological processes. These models are also critical for assessing the accuracy of numerical studies which can be a helpful tool for evaluating physical quantities not assessable *in vivo*.

**In this study we presented a methology based on fluid-structure interaction (FSI) approach for computing the structural and fluid stresses acting on the computational trachea wall *in silico* while an experimental animal study was performed in order to show *in vivo* the consequences of the implantation of these two types of stent. This comparison can only be performed on animals due to the impossibility of providing the necessary histological information in humans.** Finally, numerical and experimental findings were interpreted and compared using wall shear stress and tensile stress coming from the computational study and the inflammation, the epithelial thickening and the granulation observed in the histological sections of the explanted rabbit stented tracheas.

# 2 Materials and Methods

## 2.1 Experimental protocol, imaging acquisition and histological images analysis

The stents analyzed in this work resemble the commercial devices Zilver® Flex$^{TM}$ (Cook Medical, Bloomington, Indiana, U.S.A.) and the WallStent$^{TM}$ (Boston Scientific, Natick, MA, U.S.A.). The Zilver® Flex$^{TM}$ stent is a memory shape Nitinol laser-cut stent with a squared cross section of 100 $\mu m$. Nitinol is an alloy composed of 55% nickel and 45% titanium that exhibits a unique shape memory. This device exhibits excellent flexibility

allowing it to adapt well to the anatomical structure. The Wallstent$^{TM}$ is composed of $20-24$ stainless steel alloy filaments, each 100 $\mu m$ in diameter, organized in a crisscross pattern to form a tubular braid configuration [34]. The filament crossing points are not fixed but are free to slide or swivel over each other. This unique design allows the stent to be flexible, compressible, and able to conform to irregular airway geometry.

Each stent type was implanted in 10 one year old New Zealand white rabbits (*Oryctolagus cuniculus*). A group of 10 was intentionally left without stent and treated as the "control group". New Zealand white rabbit was chosen because it is manageable, presents a low cost and is often used in experimental study due to the similarity of its tracheal wall to that of humans [35]: in particular, as documented in the literature, rabbit model has been previously used for analyzing the interaction between tracheobronchial stent and tracheal tissue [36,37,38]. In order to justify the choice of rabbit as the animal for the study, prior to this study, an histological comparison between human and tracheal tissue was performed. Both trachea showed similarities from a histological point of view, which allow the extrapolation of the present results to humans. **The New Zealand rabbit demonstrates an important and rapid airway response, which is considered an advantage for investigations in the field of the stenting technique [39]. Its epithelium is highly reactive, especially in presence of a foreign body. This aspect facilitates tissue reaction such as epithelial thickening and granulation after prosthesis insertion. These biological processes are welcome processes for studying the tissue reaction promoted by the insertion of a medical device.**

**The main differences between human and rabbit trachea** can be found under geometrical point of view. The human trachea, for instance, is proportionally shorter with respect to the rabbit trachea. The corresponding tracheal thicknesses and luminal diameters are also different. Also the shape and the total number of cartilage rings and transversal muscle dimensions are different. Some additional details will be given in the next section. The implantation of the prostheses was carried out following the rules of the Ethical Committee of the University of Zaragoza (identification number of the positive votum $PI23/08$).

Computerized tomography of the rabbits was performed by means of Philips Brilliance 16P equipment. In particular, topographic longitudinal and helicoidal data acquisition was realized from cranial to thorax section.

High resolution CT-scans of 1 $mm$ thick and 0.5 $mm$ interslice distance were obtained with 120 $Kvp$ and $248mA$ X-rays intensity. Animals were sacrificed by an intravenous sodium pentobarbital injection 90 days post-implantation. An endoscopic examination was performed after rabbit sacrifice. The 30° and 4 mm optic (Karlz Storz, Hopkins II, GmbH & Co. KG Tuttlingen, Deutschland) was introduced through an incision at the cricothyroid ligament to assess tracheal response. The trachea was extracted, fixed in 10% formaldehyde and embedded in methacrylate resin to be excised by a microtome Exact (Zeiss, Jena, Germany). Finally, histomorphometric analysis was performed. Consecutive thick sections of 5 $mm$ were obtained and numbered from proximal to distal ends. Each section was then ground to $3-5$ $\mu m$ and stained with Hematoxylin - Eosin (H - E) for histological analyses. The histology was carried out by means of a microscopy Nikon Eclipse 80i with a coupled Nikon digital camera DXM1200C and the program Nikon ACT-1C Software 1.02, analyzing the following parameters: epithelial thickening, acute inflammation and presence of granuloma. The level of tissue inflammation was evaluated in the histology analyzing the concentration of inflammatory cells such as neutrophil, macrophage, monocyte, eosinophil, basophil which participate in the inflammatory response to a foreign body or substance. Epithelial thickening was classified in 4 levels depending on size: without thickening ($50$ $\mu m$), light thickening ($> 50-100$ $\mu m$), moderate thickening ($> 100-150$ $\mu m$), severe thickening ($> 50$ $\mu m$). Wall thickening, granuloma and inflammation were compared and interpreted with the results provided by the FSI simulations which provided information of both structural and fluid parts. **The computational models of the coupled solid and fluid of the healthy and stented rabbit trachea are shown in Figure 1 (a), (b) and (c)**. Distributions of solid and fluid stimuli derived from numerical simulations were compared with the biological response measured in transverse histological sections taken along the length of the stented region. The consequences of the stent implantation were quantified from histology at selected cross-sections depicted in Figure 3 (c). This Figure shows histological data from three cross-sections collected at proximal, middle and distal location with respect to the stent. Sections were selected to illustrate the variation of inflammatory processes, tissue thickening and the possible formation of granuloma along the devices.

## 2.2 Idealized trachea model

The trachea of both humans and rabbits is made up of hyaline cartilage rings, a dorsal membrane and epithelium. The difference is that the human cartilage rings are $C$-shaped, whereas in rabbits the rings are almost complete. Besides, trachea of the rabbit is proportionally longer than the human trachea because it has a length of $6 - 8\ cm$[35]. The human trachea is $10 - 16\ cm$ long. Naturally the corresponding tracheal thicknesses and diameters are also different. The main dimensions of the idealized trachea were established based on the samples of the "control group". The cartilaginous rings and muscular membrane with their corresponding thicknesses were detected and measured. A constant wall thickness of $0.8\ mm$ was measured from the dissected sample of the control group. A cartilagineous ring and a membrane width of $3\ mm$ and $2\ mm$ respectively were also found. Finally a muscular membrane width of $2.5\ mm$ was measured. The details of the healthy trachea are reported in Figure 1 a). The diameter of the healthy trachea was measured from the CT-images. In particular, a diameter of $5.5\ mm$ was found. In the numerical simulations, also based on the CT-images, it was assumed that the diameter was constant along the stent length. The CT scans for the healthy trachea are shown in the Figure 2 a). Starting from the reconstruction, performed by means of the software package MIMICS (Materialise Software, Leuven, Belgium), the idealized model was approximated as a cylindrical tube (the Figure refers to the fluid part). Due to the curvature of the healthy rabbit trachea, the tracheal tube considered for the measurements is the almost straight tract indicated in the Figure. Finally, the length of the rabbit trachea was measured. The distance between cricoid and carina was $7\ cm$.

## 2.3 Stent models

The Zilver® Flex$^{TM}$stent is a self-expandable Nitinol wired stent with a zigzag configuration. Its geometry was reconstructed using the commercial computer aided design (CAD) software Rhinoceros (Robert McNeel & Associates, Seattle, WA, USA) so that the internal diameter, thickness and length were modeled with the same tubing size corresponding to real manufacturing dimensions. The final expanded configuration was obtained through the medical images corresponding to the trachea rabbit geometry after stent implantation. **Firstly**

**the stents are geometrically built inside the unloaded configuration of the trachea which is a tube with a constant diameter. Both correspond to a continuous solid mesh with the solid domain of the trachea. This means that these are initially attached to the trachea (see Figure 1 - (b) and (c)). Then, the two devices were opened during the simulations till the desired diameter, using the medical images. The stent and the trachea are still attached and since no contact surface is defined, these stay attached also during the simulation of the natural breathing (see Figure 1 - (b) and (c)).** As documented in literature[40,41], nitinol shape memory alloys undergo a phase transformation in their crystal structure when cooled from high temperature (austenite) to low temperature (martensite). When shape memory alloys are in their martensitic form, they are easily deformed to a new shape. However, when the alloy is heated, it reverts to austenite and recovers its previous shape with great force (process known as shape memory). This inherent phase transformation determines the special characteristics of these alloys: shape memory and superelasticity. Martensite and austenite possess a different mechanical behavior characterized by a different Young modulus (32 $GPa$ and 40 $GPa$ respectively[40]). Since we are not interested in the opening process of the stent, for describing the mechanics of this device we adopted the elastic behavior, using the austenite Young modulus (see Table 1). The Wallstent$^{TM}$ is made up of thin Elgiloy® stainless steel wire mesh, relying on predetermined spring like design to achieve desired expansion. Wallstents$^{TM}$ are compressed within a delivery catheter, which is an integral part of the delivery system. The external catheter maintains the collapsed state of the stent until its retraction allows the device to expand. Device deployment is carried out by retracting the outer sheath while holding the stent in place with the inner tube. For its modeling, we adopted the elastic behavior of the stainless steel. The Young modulus and Poisson's ratio are summarized in Table 1. Finally it should be noted that for reasons of computational costs, as mentioned above, only a portion of the stents in longitudinal direction was modeled. Only a reduced number of stent struts were considered more in details, rather than the entire number along the length. In particular, a stent length of 1 $cm$ for both devices was modeled. In radial direction the entire strut was reconstructed for both stents. The reconstruction based on CT scans is shown for the Zilver® Flex$^{TM}$ stent in Figure 2 b).

## 2.4 FSI computational models

The FSI simulations were undertaken using an individual tracheal idealized model, the dimensions for which were extracted from micro-CT images. A luminal diameter of $5.5mm$ was obtained from computerized tomography of the rabbit trachea as well as cartilaginous rings and muscular membrane with their corresponding thicknesses (see Figure 1 a)). A constant wall thickness of $0.8mm$ was measured from the dissected sample of the control group. The stress-free diameter of the numerical model corresponds to the diameter measured from the available CT images. The geometrical model of the healthy trachea was built using the commercial software Rhinoceros. The two stent types were reconstructed both with their real dimensions using squared sections, approximating, for sake of simplicity, the WallStent$^{TM}$ stent, the section for which is originally circular. This significant assumption, **that certainly influences the computational results since it causes a stiffer geometrical configuration** was necessary to model the problem as FSI due to the complexity of making contact between stent and tracheal wall in the presence of the fluid. With the same software package, the two stent types were built and inserted in the initial undeformed configuration of the trachea. In this way we obtained three geometrical models (healthy trachea, trachea with ZilverFlex$^{TM}$ Stent and trachea with WallStent$^{TM}$) which were later imported in the commercial software Ansys Icem (Ansys Inc. Software, Canonsburg, PA, USA) for the creation of the numerical grids. The tracheal lumen was meshed using tetrahedral elements, due to the complexity of the stented geometries. While for the healthy trachea a mesh of around $1.5 \cdot 10^6$ elements was reached ($10^6$ elements for the fluid part and 500000 elements for the solid part), for the stented geometries the grid sizes were $3 \cdot 10^6$ ($1.5 \cdot 10^6$ elements for the fluid and for the solid part respectively). Details of the meshes near the stent struts are shown in Figure 3 (a) and (b). Prior to this final grid creation, a mesh independence study was carried out and the necessary grid size was established. The solid grid was built simultaneously with the fluid mesh so that the cells number was created accordingly with the fluid cell number and it is sufficiently fine to obtain the displacements of the present problem [40] .

## 2.5 Experimental tensile test

To determine the real properties of the different tissues of the rabbit trachea we followed the same procedures as explained in a previous study[20]. Four rabbit tracheas were considered in the experimental analysis and three samples for each trachea were dissected for tensile tests and mechanical analysis procedures. No significant differences ($p > 0.5$) were found between uniaxial tested samples and significant differences ($p < 0.01$) were found between cartilage and muscle. The tracheal rabbit specimens were mounted on the Instron MicroTester 5548 (Instron® Corporation, Norwood, MA, USA) to perform uniaxial tensile tests. In the cartilage rings, no preferential orientations were found since the collagen fibers run randomly. This tissue behavior was then modeled in the commercial software by means of an isotropic material model. The muscular membrane, due to the small tensile stresses acting on the rabbit trachea, was modelled as well as isotropic. Comparing rabbit trachea with human trachea (which presents an anisotropic behavior), the stress range working on the muscular membrane is almost ten times smaller[26,42]. For both cartilage and muscle, since no preferential orientation was revealed, the Demiray strain energy density function $W = D_1 \left[ exp\left(D_2(\overline{I}_1 - 3)\right) - 1\right] + U(J)$ was used to fit the experimental results. In this function $\overline{I}_1$ is the first invariant of the deviatoric right Cauchy-Green tensor $\overline{\mathbf{C}} = J^{-2/3}\mathbf{F}^T\mathbf{F}$, $J = det(\mathbf{F})$ is the Jacobian, $\mathbf{F}$ is the standard deformation gradient, $U$ is the volumetric energy function and $D_1$, $D_2$ are material constants summarized in Table 2.

## 2.6 Boundary conditions for the FSI simulations

Air flow was modeled as an incompressible (density $\rho = 1.225\ kg/m^3$), and Newtonian fluid (viscosity $\mu = 1.83 \cdot 10^{-5}\ kg/m \cdot s$)[43]. As usual for FSI studies, mixed boundary condition types are necessary for correctly computing velocity field and tensile stresses and strains. To simulate rabbit breathing, we used pulsatile waveforms for velocity and pressures, the maximal value of which were evaluated through a spirometry performed on the rabbit by means of the commercial equipment Datex Ohmeda 7100 anaesthetic machine (Datex-Ohmeda Inc., Madison, WI, USA). In particular, the maximal/minimal peak pressure resulted in 2 $cmH_2O$ while the peak flow velocity resulted 0.4 $m/s$ (see Figure 4). The geometry and inlet conditions specified above result in

a maximum Reynolds number of $Re = 147.27$ justifying the assumption of laminar flow. The coupled scheme was used for pressure-velocity coupling, and second-order upwind discretization was used for the momentum transport equations. Convergence was achieved for continuity and momentum when residuals fell below $10^{-6}$. The time step size was set to $0.001s$ after an appropriate temporal sensitivity analysis. The computations were carried out using the 8 noded, Dual Nehalem (64 bits), 16 processor cluster with a clock speed of 2.33 $GHz$ and 32 $Gb$ memory for each node.

## 2.7 Simulations of the stent opening and FSI computations

The numerical simulations were carried out with the commercial software Adina $R\&D$ Inc. (Watertown, MA, USA). The fluid-solid coupling used by this software is extensively explained in literature [44] and it was explained in detail in previous studies [26,42]. The fluid and solid grids for each computed case were imported separately in the software. Then, the computational models, consisting of separated merging computational meshes, constitutive fluid and structural models and the boundary conditions, were created. The software package provides strong coupling between fluid and solid domain and used linear elements. First, the simulation of the healthy trachea model was carried out. Then, by means of two separate FSI analyses, the two stent types were opened under displacement control untill the desired final diameter, i.e. the final open configuration which was previously measured using the CT-images and the commercial software MIMICS, is reached. Table 3 summarizes the main geometrical information of the commercial stents. Furthermore, these configurations were used as initial configuration for the breathing cycle of the rabbit. In particular, in order to avoid losing the initial stresses due to the opening phase, which represent the highest stresses at the stented tracheal wall, the breathing cycle was started in the same simulation after stent deployment. **At this stage, during the respiratory cycle, the displacements used to open the two stents are still applied in order to avoid the elastic recoil to their initial state. In other words, the two stents in their initial configuration, which corresponds to the tracheal diameter, are attached to the tracheal tube (see Figure 1 - (b) and (c)). Then the deployment is conducted under displacements control till the final configuration**

**is reached. Finally, the reached displacements are still applied to hold the stents open during the entire breathing cycle. Thus, the device behaves as a rigid body during the simulation of the respiration.** The boundary conditions for the respiration described in the previous section were applied for the three models at the inlet and outlet. Since velocity and pressure were applied by means of flat profiles, to guarantee fully developed flow inside the healthy and stented trachea, the inlet and outlet of the fluid and solid numerical model were extruded. The length of these extrusions was taken as 5 times the diameter of the trachea as performed in previous studies[45,42]. This yields to a length of 27.5 $mm$ for each inlet and for each outlet extension.

# 3 Results

The final open configuration for both stents, just at the beginning of the respiration, is represented in Figure 1 b) for the Wallstent$^{TM}$ and in Figure 1 c) for the Zilver® Flex$^{TM}$ stent. Starting from these geometries, i.e. once the final displacement was reached, the velocity and pressure waveforms shown in Figure 4 started. Five variables were considered: three experimental variables for evaluating the biological response (inflammation, epithelial thickening and granulation) and two numerical variables which represent the mechanical (maximum principal stress) and fluid (WSS) stimuli acting on the vessel wall.

The presence of a stent inside the tracheal segment significantly alters the air flow patterns. This is shown in Figure 5 where the fluid dynamics results are compared for healthy (sub figure 5 a)) and stented tracheas (sub figures 5 b) and c)). The left side of Figure 5 shows the velocity magnitude along a longitudinal plane at peak flow during inspiration for the healthy (sub figure 5 a)) and stented tracheas (sub figures 5 b) and c)). An abrupt reduction of fluid velocity occurs when the airflow crosses the stented segment of the trachea because of the rapid change in cross-section between the inflow region and the stented zone. The right panel of Figure 5 shows how the spatial distribution of WSS is affected by the presence of the devices. Different patterns are visible for healthy (sub figure 5 a)) and stented tracheas (sub figures 5 b) and c)). **While for the**

**healthy tracheal wall a uniform WSS distribution is shown (Figure 5 a), an altered shear stress distribution with low values is visible in the stented region near the stent struts (sub-figure 5 b) and c))**. High values are located at the entrance and exit segments of the stented computational domain. At the center of the stent cells, where the tracheal prolapses into the lumen causing a sudden reduction of cross-sectional area, the WSS assumes higher values in comparison to the regions near the stent struts. The **low WSS distribution around the stent struts** suggests that zones at highest risk of epithelial growth are located along the stented region. **This is visible comparing the healthy and the stented trachea (Figure 5). This aspect is well stated in the literature[21,22,23] for the cardiovascular field and can be confirmed here for tracheobronchial prosthesis. The alteration of the WSS spatial distribution is primarely due to the overexpansion of the stent** which results in an abrupt enlargement of the tracheal section. **This enlargement affects as expected also the tensile stresses as evidenced when looking at the map of maximal principal stress for the two types of prosthesis.** In Figure 6, 7 and 8, the numerical results are compared with the endoscopic images and with the histology for the healthy trachea, the WallStent$^{TM}$ and the Zilver® Flex$^{TM}$ respectively. Figure 6 b) and c) revealed that, as to be expected, no abnormal growth or inflammation were present in healthy tracheal rabbit; this ensures that any alterations affecting the other two groups of animals were due only to the implantation of the device. In Figure 7 a) the tensile stresses at peak inspiration are compared with the endoscopic images (sub figure 7 b)) which reveals re-epithelialization around the stent struts for the Zilver® Flex$^{TM}$ stent (white region indicated with a blue arrow in sub-figure b)). It should be noted that, in the animal study, 100% of analyzed tracheal slices for the Zilver® Flex$^{TM}$ stents showed complete re-epithelialization. This is confirmed by the histology shown in Figure 7 c). On the other hand, for the WallStent$^{TM}$ only partial re-epithelialization was found, in addition to granuloma developed at the end of the device at distal stent section (indicated in Figure 8 b) and c) with a blue and a red arrow respectively). **Interestingly, in the computational study, at the same location we found higher stresses at the end of the WallStent$^{TM}$ than those found for the Zilver® Flex$^{TM}$ stent (see Figures 7 a) and 8 a)). One of the possible reasons of this difference could be related**

**to the geometry of both stents**. The WallStent$^{TM}$ presents in fact an open-strut structure at its ends which may promote damage on the tracheal tissue. Considering the sections represented in Figure 3 c), 71.4% of the analyzed tracheal slices presented granuloma at the ends of the WallStent$^{TM}$ (57.1% at the proximal and 42.9% at distal section). Suspected presence of granuloma was also found in the endoscopic images for the Zilver® Flex$^{TM}$ in 55.6% of the analyzed sections at the same locations, however, the histology only confirmed 12.5% of cases. Figure 7 b) and e) shows the absence of granuloma found in 87.5% of the analyzed sections that can be correlated in the numerical simulation with the maximum principal stress at the ends of the device. Its values were lower with respect to those of the WallStent$^{TM}$. Figure 7 c), d), e) and 8 d), e) shows the histology for the Zilver® Flex$^{TM}$ and for the WallStent$^{TM}$ group in terms of inflammation and tissue thickening. The presence of an inflammatory process and tissue thickening is evidenced for the WallStent$^{TM}$ (sub-figure d) and e)) through the microscopic images H-E 10X while, as discussed, for the Zilver® Flex$^{TM}$ stent lower thickening and low inflammation were found (sub-figure d) and e), microscopic images H-E 10X). The inflammation level was measured through the histology evaluating the increase of wall thickness and the presence of inflammatory cells such as neutrophils and macrophages. In particular, 75% of the tracheal sections with Zilver® Flex$^{TM}$ stent showed no thickening at the central part of the stent while 60% showed it at the distal and proximal sections of the prosthesis. Thickening was low in most cases. However, in the WallStent$^{TM}$ group, all the animals developed stenosis at the proximal section of the stent. 88.9% of analyzed sections showed stenosis at the distal section.

**With respect to the Zilver® Flex$^{TM}$ stent, higher tensile stresses were also found for the WallStent$^{TM}$ within the stent cells where the trachea prolapses into the lumen (see Figures 7 a) and 8 a)). The stress map found for the WallStent$^{TM}$ is certainly influenced by the neglected sliding movement between struts in the computational study. However, the stress map indicates high values in the same regions where inflammation episodes are revealed by the histology of the stented group (see Figure 8, sub-figure d)). In Figure 8 a), the numerical results depict in fact non-homogeneous values of the maximum principal stress at longitudinal tracheal**

**cross-sections. Even considering the limitations in the computational modelling of both devices, this finding seems to indicate important consequences of the different geometrical design of the idealized WallStent$^{TM}$ in comparison to the Zilver® Flex$^{TM}$. It has to be acknowledged that the stiffness of the idealized WallStent$^{TM}$ is probably overestimated because of the modelling and the approximations taken in this work.**

# 4 Discussion

Following the recommendation of the FDA (Food and Drug Administration) [46], the insertion of a metallic stent for benign pathologies has to be conducted only when the pathology cannot be treated by other means such as surgery or insertion of silicone stents [46,47,48,49]. In literature many studies have documented good results for treatment of central lesions in the human airways for both benign and malign pathologies [12,14,15]. The use of metallic stents presents many advantages such as easily insertion by flexible bronchoscopy and good radial force which reduces the risk of migration compared to silicone prosthesis. Moreover, the re-epithelialization promoted by metallic stents restores mucous transport [2,15,1]. However, many studies do not recommend the use of metallic stent for treating benign stenosis due to the frequent inflammation and/or its predisposition to granuloma formation. This study suggests the influence of realistic 3D deployed stent geometry on the coupled structural and fluid mechanics following stent deployment. **The experimental model indicates** that the idealized WallStent$^{TM}$ seems to promote an important response of the tracheal tissue at the proximal and distal ends of the stented region with respect to the central region. This effect is not observed for the Zilver® Flex$^{TM}$ stent, probably due to the different geometrical design at their ends. **This hypothesis is supported by the numerical results at the same location in terms of maximum principal stress.** Interestingly, in the computational study, higher stresses were also found within the WallStent$^{TM}$ cells which suggests, always considering the significant assumptions made, a possible reason why this stent promotes a major degree of cellular proliferation in comparison to the Zilver® Flex$^{TM}$. **The in-stent higher stresses are probably caused**

**by the higher stiffness of the WallStent$^{TM}$ in comparison to the Zilver® Flex (Young modulus of the WallStent$^{TM}$ is two order magnitude higher than that of the Zilver® Flex$^{TM}$). It has to be noted that the WallStent$^{TM}$ is significantly more compliant than the model proposed in this work because the struts of circular cross-section can slide over one another under macroscopic deformation. For this reason, the computational result could be overestimated.**

It is important to emphasize that the epithelial hyperplasia is a complex phenomenon resulting from the interaction of multiple factors such as non physiological fluid dynamics factors on the luminal wall, abnormal stresses in the tracheal wall, injuries caused by stent deployment or structure such as the case of the WallStent$^{TM}$ and the associated inflammatory response, among other aspects. These factors are not necessarily associated to the certainty of a severe tissue response, but will probably increase the predisposition of the tracheobronchial wall to such a process. By joining histology and numerical simulations, with help of CT images it is possible to capture the stimuli between struts and the resulting correlation with local biological response. Naturally, further work will be required to evaluate the consistency of these correlations within rabbit *in vivo* models and whether these effects are observed in a clinical context. Moreover, the presented analysis seems to suggest a more important relative response promoted from the tensile stresses at the walls compared to that promoted by the wall shear stress. This means that the mechanical stimulus drives the tissue response of the stented region while fluid dynamics seems to play a less dominant role.

## 4.1 Limitations

The major limitation of this work is in the use of linear elasticity for the material model of the stents. This assumption may significantly affect the presented results, especially the presented stress values. The stent deployment procedure is approximated due to the intrinsic way in which this is numerically conducted. Since displacement control is used, no recoil is present in the models. Recoil is expected to occur with the stainless steel design and the chronic outward force of the nitinol design are not captured sufficiently with the material models used. Both stents are in fact modeled as elastic materials. This aspect further affects tissue stress

state which is highlighted by the presence of high stress level due to deployment of the devices. Moreover, the stent and the trachea were supposed to be attached to each other, thus no contact condition was defined. In this way overall stenting is further approximated. In addition, while in this work we were able to reproduce the geometrical features of the Zilver® Flex$^{TM}$ stent, the geometry of the WallStent$^{TM}$ was approximated simplifying its cross-sectional area as squared instead of cylindrical. This assumption may lead to a concentration of the stresses due to the different contact surface between device and tracheal wall. Also, for this stent type, **the wire-wire stent contact and the relative movement between wires were neglected. It is well known that generally speaking the laser-cut stent configuration is significantly stiffer than a woven/braided wire configuration (for the same material and overall geometry). This aspect certainly is contributing to the resulting high stiffness of the WallStent$^{TM}$ modeled in this study and the stresses that are generated in the tissue. The WallStent$^{TM}$ is significantly more compliant than this model would imply because the struts/braids can slide over one another under macroscopic deformation.**

The healthy trachea was considered as a cylindrical tube. In this way, the curvature which characterized the rabbit trachea was neglected. Finally, the computational models should be validated against experimental bench testing (for example radial force testing of the crimp and deployment of the stents) to assess the accuracy of in-vivo stent behavior. This validation cannot be performed in this work and it is left for further studies.

The presented results, are obtained using trachea models. The computational costs, already high, would massively increase in the case of real geometries and complete stent geometries. However, it is clear that idealized models may not disregard important details which may affect the overall results. In this study we have focused our attention on the methodology to compare *in silico* with *in vivo* observations and we have demonstrated that an idealized model is capable of giving an initial insight in the associated biological processes.

# 5 Conclusions

This computational study considers the structural and fluid dynamic stimuli acting on a stented trachea in the post-deployment configuration of two different types of device, using a fluid-structure interaction approach. The available histological data provides an insight into the relationship between these factors and biological processes such as inflammation, epithelial thickening and granulation. The computational results support the combined role of both structural and fluid mechanics to determine the magnitude of tissue response with the structural mechanics that seems largely dominant. Numerical results indicate in fact a different behavior **in terms of stress distributions** for the two commercial stents while the associated WSS distributions are relatively similar in both cases. By way of conclusion, **after the experimental work the WallStent$^{TM}$ seems to be more prone to produce abnormal tissue growth and this result is supported by the numerical study. The** comparison between idealized models and experimental findings indicates that the presented *in silico* model can be used to assess the features necessary for analysis of the associated biological aspects. Finally, the presented work, even with some necessary assumptions, seems to indicate a more important response promoted from the tracheal stresses as a reaction to stent insertion than that promoted by the associated fluid dynamics.

# Ethical Standards

All institutional and national guidelines for the care and use of laboratory animals were followed and approved by the appropriate institutional committees. The work reported in this manuscript does not involve human subjects.

# Conflict of interest

None of the authors of this work has conflict of interest with other people and organizations.

# Acknowledgments

This study was supported by the CIBER-BBN financed by the Instituto de Salud Carlos III with assistance from the European Regional Development Fund and by the Spanish Ministry of Science and Technology through Research Project DPI2013-44391-P. The experimental study was supported by the Instituto de Salud Carlos III, through research project PI08/1424 and was performed by the Minimally Invasive Techniques Research Group (GITMI) of Aragón Government.

# References

[1] S. Fernandez Bussy, O. Akindipe, V. Kulkarni, W. Swafford, M. Baz, M. A. Jantz, Clinical experience with a new removable tracheobronchial stent in the management of airway complications after lung transplantation, Journal of Heart Lung Transplant 28(7) (2009) 683–688.

[2] A. L. Rafanan, A. C. Mehta, Stenting of the tracheobronchial tree, Radiologic Clinics of North America 38(2) (2000) 395–408.

[3] F. Dumon, A dedicated tracheobronchial stent, Chest 97 (1990) 328–332.

[4] O. Fruchter, Y. Raviv, B. D. F. Kramer, Removal of metallic tracheobronchial stents in lung transplantation with flexible bronchoscopy, Journal of Cardiothoracic Surgery 12(5) (2010) 72.

[5] A. Dasgupta, B. L. Dolmatch, W. J. A.-S. P. N. M. A. C. Mehta, Self-expandable metallic airway stent insertion employing flexible bronchoscopy: preliminary results, Chest 114(1) (1998) 106–109.

[6] F. Sun, J. Uson, J. Ezquerra, V. Crisostomo, L. Luis, M. Maynar, Endotracheal stenting therapy in dogs with tracheal collapse, The Veterinary Journal 175 (2008) 186–193.

[7] K. Rauber, C. Franke, W. S. Rau, Self-expanding stainless steel endotracheal stents: an animal study, Cardiovascular Interventional Radiology 12(5) (1989) 274–276.

[8] H. Hautmann, M. Bauer, K. J. Pfeifer, R. M. Huber, Flexible bronchoscopy: a safe method for metal stent implantation in bronchial disease, Annals of Thoracic Surgery 69(2) (2000) 398–401.

[9] R. M. Mroz, K. Kordecki, M. D. Kozlowski, M. D. Baniukiewicz, A. Lewszuk, Z. Bondyra, Severe respiratory distress caused by central airway obstruction treated with self-expandable metallic stents, Journal of Physiology Pharmacology 59 (Suppl 6) (2008) 491–497.

[10] M. A. De Gregorio, Prótesis traqueobronquiales en radiología intervencionista, Técnicas intervencionistas en el tórax 1st ed. Zaragoza: Aqua (2003) 343.

[11] D. Makris, C. H. Marquette, Tracheobronchial stenting and central airway replacement, Current Opinion in Pulmonary Medicine 13(4) (2007) 278–283.

[12] C. P. Saad, S. Murthy, G. Krizmanich, A. C. Mehta, Self-expandable metallic airway stents and flexible bronchoscopy: long-term outcomes analysis, Chest 124(5) (2003) 1993–1999.

[13] J. H. Kim, H. Y. Song, J. H. Park, B. D. Ye, Y. S. Yoon, J. C. Kim, Metallic stent placement in the palliative treatment of malignant colonic obstructions: Primary colonic versus extracolonic malignancies, Journal of Vascular and Interventional Radiology 22(12) (2011) 1727–1732.

[14] S. A. Husain, D. Finch, M. Ahmed, A. Morgan, M. R. Hetzel, Long-term follow-up of ultraflex metallic stents in benign and malignant central airway obstruction, Annals of Thoracic Surgery 83(4) (2007) 1251–1256.

[15] F. T. Chung, H. C. Chen, C. L. Chou, C. T. Yu, C. H. Kuo, H. P. Kuo, An outcome analysis of self-expandable metallic stents in central airway obstruction: a cohort study, Journal of Cardiothoracic Surgery 8(6) (2011) 46.

[16] J. Y. Qian, F. Zhang, B. Fan, L. Ge, Q. B. Wang, J. B. Ge, A more than 2 year follow-up of incomplete apposition after drug-eluting stent implantation, Chinese Medical Journal (English Edition) 121(6) (2008) 498–502.

[17] H. S. Gurm, T. Boyden, K. B. Welch, Comparative safety and efficacy of a sirolimus-eluting versus paclitaxel-eluting stent: a meta-analysis, American Heart Journal 155(4) (2008) 630–639.

[18] C. Stettler, S. Wandel, S. Allemann, A. Kastrati, M. C. Morice, A. Schoemig, M. E. Pfisterer, G. W. Stone, M. B. Leon, J. S. de Lezo, J. J. Goy, S. J. Park, M. Sabaté, M. J. Suttorp, H. Kelbaek, C. Spaulding, M. Menichelli, P. Vermeersch, M. T. Dirksen, P. Cervinka, A. S. Petronio, A. J. Nordmann, P. Diem, B. Meier, M. Zwahlen, S. Reichenbach, S. Trelle, S. Windecker, P. Jueni, Outcomes associated with drug-eluting and bare-metal stents: a collaborative network meta-analysis, Lancet 370(9591) (2007) 937–948.

[19] M. Malvè, I. Barreras, J. L. López-Villalobos, A. Ginel, M. Doblaré, Computational fluid-dynamics optimization of a human tracheal endoprosthesis, International Communication in Heat and Mass Transfer 39 (2012) 575–581.

[20] M. Malvè, C. Serrano, R. Fernández-Parra, E. Peña, F. Lostalé, M. A. D. Gregorio, M. A. Martínez, Modeling the air mass transfer through a healthy and a stented rabbit trachea: CT-images, computer simulations and experimental study, International Communication in Heat and Mass Transfer 53 (2014) 1–8.

[21] R. Balossino, F. Gervaso, F. Migliavacca, G. Dubini, Effects of different stent designs on local hemodynamics in stented arteries, Journal of Biomechanics 41(5) (2008) 1053–1061.

[22] C. Chiastra, S. Morlacchi, S. Pereira, G. Dubini, F. Migliavacca, Computational fluid dynamics of stented coronary bifurcations studied with a hybrid discretization method, European Journal of Mechanics B/Fluids 35 (2012) 76–84.

[23] S. Morlacchi, B. Keller, P. Arcangeli, M. Balzan, F. Migliavacca, G. Dubini, J. Gunn, N. Arnold, A. Narracott, D. Evans, P. Lawford, Hemodynamics and in-stent restenosis: Micro-ct images, histology, and computer simulations, Annals of Biomedical Engineering 39(10) (2011) 2615–2626.

[24] B. K. Keller, C. M. Amatruda, D. R. Hose, J. Gunn, P. V. Lawford, G. Dubini, F. Migliavacca, A. J. Narracott, Contribution of mechanical and fluid stresses to the magnitude of in-stent restenosis at the level of individual stent struts, Cardiovascular Engineering and Technology 5(2) (2014) 164–175.

[25] B. D. Gogas, C. V. Bourantas, H. M. Garcia-Garcia, Y. Onuma, T. Muramatsu, V. Farooq, R. Diletti, R. J. M. van Geuns, B. de Bruyne, B. Chevalier, L. Thuesen, P. C. Smits, D. Dudek, J. Koolen, S. Windecker, R. Whitbourn, D. McClean, C. Dorange, K. Miquel-Hébert, S. Veldhof, R. Rapoza, J. A. Ormiston, P. W. J. C. Serruys, The edge vascular response following implantation of the absorb everolimus-eluting bioresorbable vascular scaffold and the XIENCE V metallic everolimus-eluting stent. first serial follow-up assessment at six months and two years: insights from the first-in-man ABSORB Cohort B and SPIRIT II trials, EuroIntervention 9(6) (2013) 709–720.

[26] M. Malvè, A. Pérez del Palomar, J. L. López-Villalobos, A. Ginel, M. Doblaré, FSI analysis of the coughing mechanism in a human trachea, Annals of Biomedical Engineering 38(4) (2010) 1556–1565.

[27] M. Malvè, A. Pérez del Palomar, A. Mena, O. Trabelsi, J. L. López-Villalobos, A. Ginel, F. Panadero, M. Doblaré, Numerical modeling of a human stented trachea under different stent designs, International Communication in Heat and Mass Transfer 38(7) (2011) 855–862.

[28] N. Charokopos, C. N. Foroulis, E. Rouska, M. N. Sileli, N. Papadopoulos, C. Papakonstantinou, The management of post-intubation tracheal stenoses with self-expandable stents: early and long-term results in 11 cases, European Journal of Cardiothoracic Surgery 40(4) (2011) 919–924.

[29] A. H. Gaafar, A. Y. Shaaban, M. S. Elhadidi, The use of metallic expandable tracheal stents in the management of inoperable malignant tracheal obstruction, European Archives of Otorhinolaryngology 269(1) (2012) 247–253.

[30] D. E. Tsakayannis, A. M. Siddiqui, H. Kozakewich, K. K. Nobuhara, J. C. Ibla, S. D. Perry, C. W. Lillehei,

The use of expandable metallic stents for acute tracheal stenosis in the growing lamb, Pediatric Surgery 33(7) (1998) 1038–1041.

[31] J. L. Ruegemer, J. A. Perkins, K. S. Azarow, L. K. O'Bryant, R. E. Nielsen, R. W. Thomas, Effect of the Palmaz balloon-expandable metallic stent in the trachea of pigs, Otolaryngology Head Neck Surgery 121(1) (1999) 92–97.

[32] S. Sawada, Y. Tanabe, Y. Fujiwara, T. Koyama, N. Tanigawa, M. Kobayashi, Y. Katsube, H. Nakamura, Endotracheal expandable metallic stent placement in dogs, Acta Radiology 32(1) (1991) 79–80.

[33] Y. Tanabe, Expandable metallic stent placement in the tracheobronchial tree in dogs, Radiation Medicine 11(6) (1993) 224–230.

[34] F. Joffre, H. Rousseau, Z. Qian, R. Chemali, Vascular stent-stent techniques: Part 2. Self-expandable intravascular stent: long-term results, Interventional Radiology. Williams & Wilkins, 1997.

[35] M. C. Jones, F. A. Rueggeberg, H. A. Faircloth, A. J. Cunningham, C. M. Bush, J. D. Prosser, J. L. Waller, N. G. Postma, P. M. Weinberger, Defining the biomechanical properties of the rabbit trachea., Laryngoscope 124(10) (2014) 2352–2358.

[36] J. Guo, G. Teng, G. Zhu, S. He, G. Deng, J. He, Self-expandable stent loaded with 125i seeds: Feasibility and safety in a rabbit model, European Journal of Radiology 61(2) (2007) 356–361.

[37] L. Novotny, M. Crha, P. Rauser, A. Hep, J. M. A. Necas, D. Vondrys, Novel biodegradable polydioxanone stents in a rabbit airway model, The Journal of Thoracic and Cardiovascular Surgery 143(2) (2012) 437–444.

[38] E. J. Vrijhof, A. de Bruïne, A. A. B. Lycklama, A. Nijeholt, L. H. Koole, A polymeric mini-stent designed to facilitate the vasectomy reversal operation. a rabbit model study, Biomaterials 25 (2004) 729–734.

[39] N. A. Kamaruzaman, E. Kardia, N. Á. Kamaldin, A. Z. Latahir, B. H. Yahaya, The rabbit as a model for studying lung disease and stem cell therapy, BioMed Research International 2013 (2013) 1–12.

[40] A. García, E. Peña, M. A. Martínez, Influence of geometrical parameters on radial force during self-expanding stent deployment. Application for a variable radial stiffness stent, Journal of the Mechanical Behaviour of Biomedical Materials 10 (2012) 166–175.

[41] C. Kleinstreuer, Z. Li, C. Basciano, S. Seelecke, M. Farber, Computational mechanics of nitinol stent grafts, Journal of Biomechanics 41 (2008) 2370–2378.

[42] M. Malvè, A. Pérez del Palomar, O. Trabelsi, J. L. López-Villalobos, A. Ginel, M. Doblaré, Modeling of the fluid-structure interaction of a human trachea under different ventilation conditions, International Communication in Heat and Mass Transfer 38 (2010) 10–15.

[43] R. K. Calay, J. Kurujareon, A. E. Holdo, Numerical simulation of respiratory flow patterns within human lungs, Respiratory Physiology and Neurobiology 130 (2002) 201–221.

[44] K. J. Bathe, Theory and Modeling guide, vol. I and II: ADINA and ADINA-F, 2006.

[45] M. Malvè, A. Pérez del Palomar, S. Chandra, J. L. López-Villalobos, E. Finol, A. Ginel, M. Doblaré, FSI analysis of a human trachea before and after prosthesis implantation, Journal of Biomechanical Engineering 133 (2011) 0710031–12.

[46] Food and drug administration. FDA public health notification: complications from metallic tracheal stents in patients with benign airway disorders, URL: *http://www.fda.gov/MedicalDevices/Safety/AlertsandNotices/PublicHealthNotifications/ucm062115.htm.*

[47] L. M. Seijo, J. Ancochea, In search of the ideal tracheobronchial stent: metal or silicone?, Archivos de Bronconeumología 40(7) (2004) 293–294.

[48] Y. Saito, H. Imamura, Airway stenting, Surgery Today 35(4) (2005) 265–270.

[49] H. Dutau, Airway stenting for benign tracheal stenosis: what is really behind the choice of the stent?, European Journal of Cardiothoracic Surgery 40(4) (2011) 924–925.

# Tables

| **Material Parameters** | $E(kPa)$ | $\nu(-)$ |
|---|---|---|
| **Nitinol (Zilver® Flex$^{TM}$ Stent)** | $40 \cdot 10^6$ | 0.33 |
| **Elgiloy (WallStent®)** | $2.1 \cdot 10^8$ | 0.3 |

Table 1. Parameters of the constitutive model that characterize the mechanical behavior of the stents.

| **Material Parameters** | $D_1(kPa)$ | $D_2(-)$ | $D(kPa)$ |
|---|---|---|---|
| **Cartilage** | 0.715 | 24.71 | 17.59615 |
| **Muscular Membrane** | 0.0084 | 14.2727 | 0.11989068 |

Table 2. Experimentally obtained parameters used to characterize the behavior of cartilage and muscular membrane: $D_1$ and $D_2$ are the model constants and $D$ the incompressibility.

| **Models** | $D_{crimp}$ $[mm]$ | $D_{free}$ $[mm]$ | ${D_{int}}^u$ $[mm]$ | ${D_{int}}^d$ $[mm]$ | **Thickness** $[mm]$ | **Length** $[mm]$ |
|---|---|---|---|---|---|---|
| **Zilver® Flex$^{TM}$ Stent** | 2.0 | 8.0 | 5.5 | 6.5 | 0.1 | 41 |
| **WallStent®** | 2.67 | 8.0 | 5.5 | 6.5 | 0.1 | 40 |

Table 3. Main geometrical characteristics of the stent models: $D_{crimp}$ refers to the crimped configuration, $D_{free}$ refers to the free diameter, ${D_{int}}^u$ and ${D_{int}}^d$ refer to the diameter before and after deployment respectively.

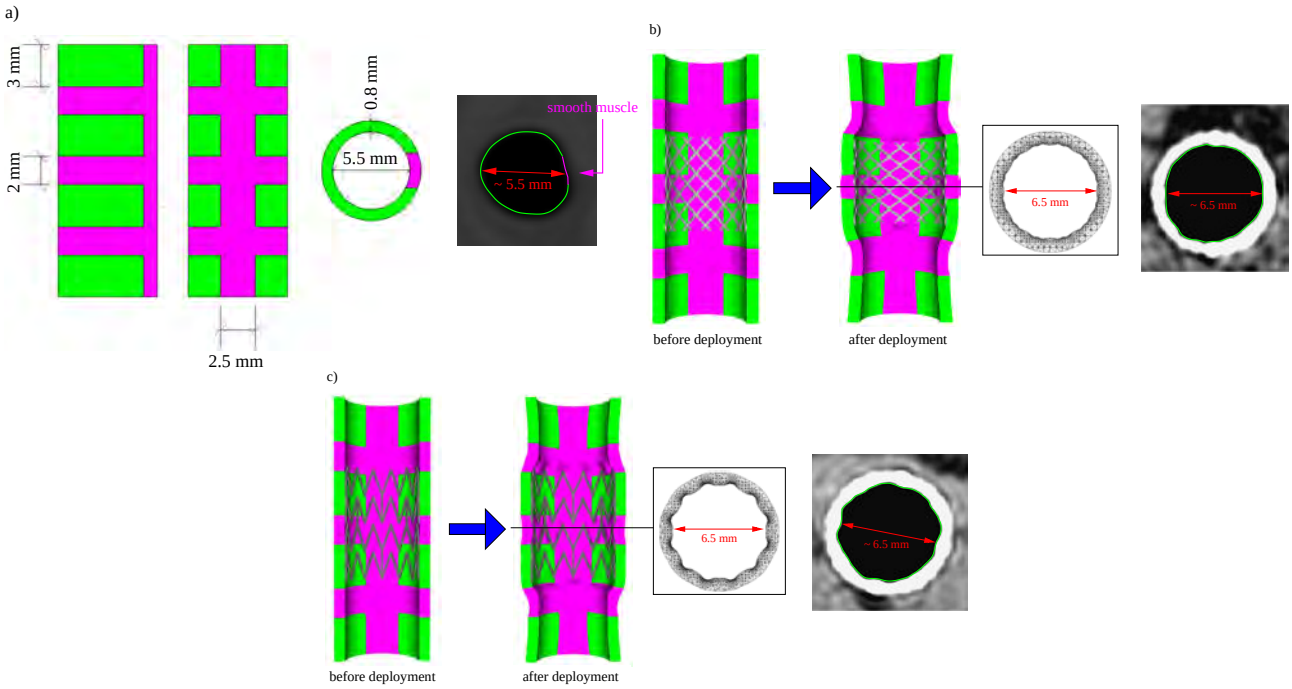


Figure 1. Stent deployment: in the left panel the healthy trachea (a), in the center panel (c) trachea with Zilver® Flex$^{TM}$ stent, in the right panel (b) trachea with WallStent$^{TM}$. **In the panels (b) and (c) the stents geometry is shown before and after deployment i.e. in its initial and final configuration.** In each model the cartilage is colored in green, the muscular membrane in purple. In the sub-figures, the healthy and stented tracheal sections coming from the CT scans and from the computations are compared with the corresponding CT-data.

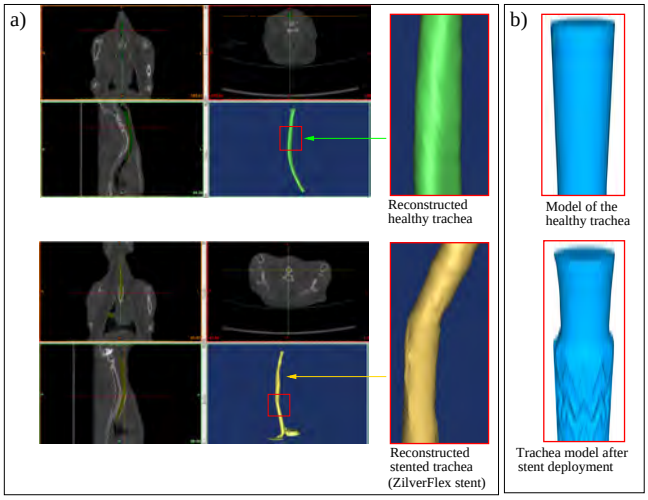


Figure 2. CT-based reconstruction of the healthy (top panel) and stented trachea (bottom panel). The stented trachea referes to the Zilver® Flex$^{TM}$ stent. In sub-figure a) the healthy and stented CT data are shown. In sub-figure b) the models used for the computational study are shown.

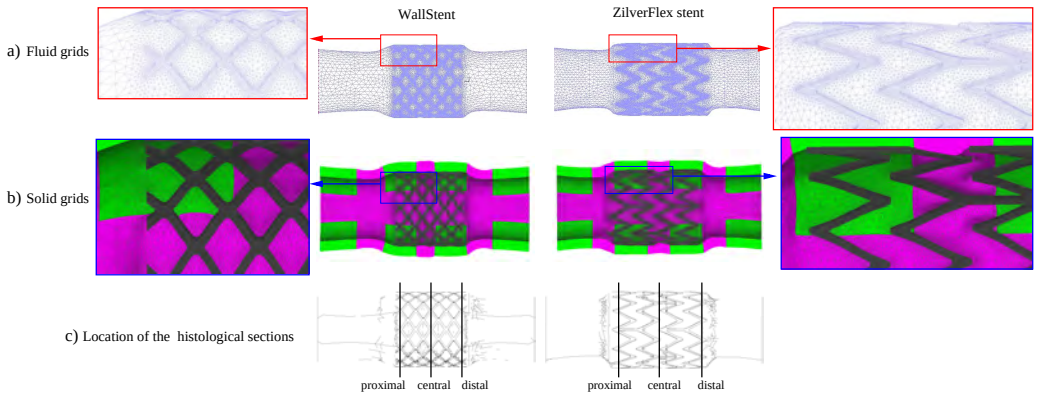


Figure 3. Numerical grids for the fluid (a) and for the solid domain (b) with close-up view on the stent refinements. In the lower panel (c) the locations of the histological sections used for the numerical-experimental comparison are sketched on the outlined stented tracheas.

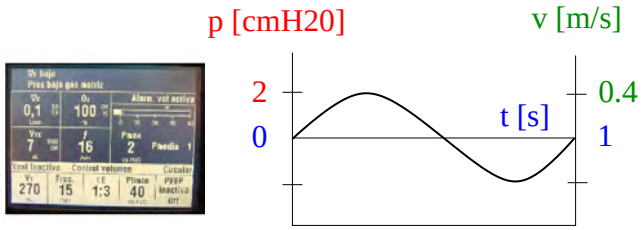


Figure 4. Flow and pressure waveforms acquired from patient specific spirometry.

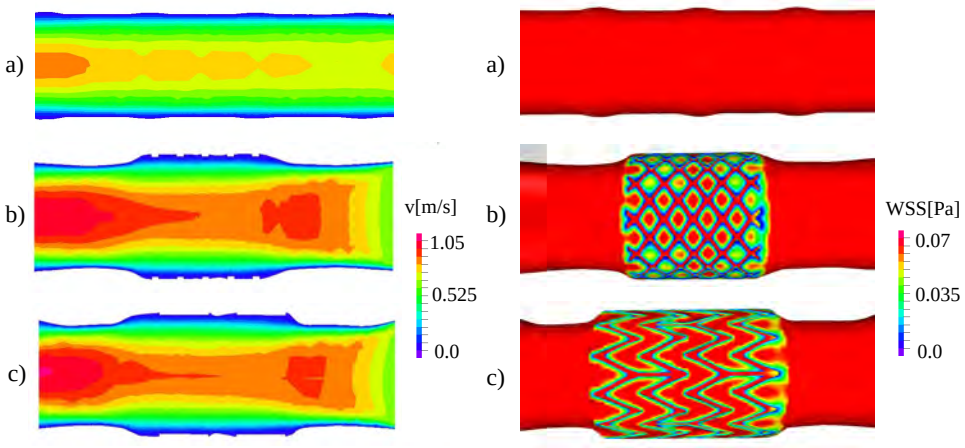


Figure 5. Contours of velocity magnitude (left panel) over a longitudinal plane of the healthy (a) and stented tracheas ((b) and (c)). Velocity perturbations caused by the presence of the stent are enhanced at the tracheal wall. Different areas of low velocity are observed for the two types of device (WallStent$^{TM}$ (b), Zilver® Flex$^{TM}$ stent (c)). Spatial WSS distribution (right panel) for healthy trachea (a), WallStent$^{TM}$ (b) and Zilver® Flex$^{TM}$ (c) at peak flow inspiration. Local alterations of the WSS around the stent struts are visible.

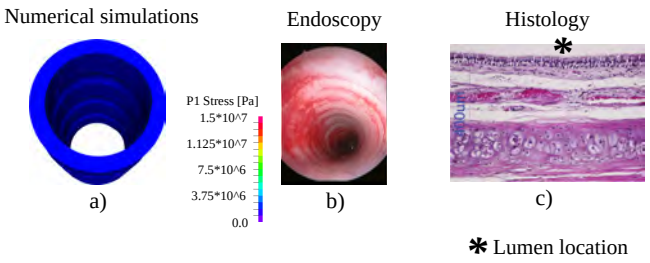


Figure 6. Comparison between numerical results (a), endoscopic images (b) and histology (c) for the healthy trachea.

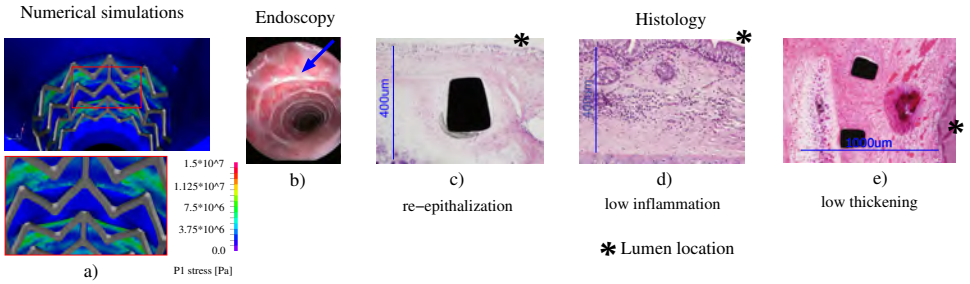


Figure 7. Comparison between numerical results at peak flow during inspiration (a), endoscopic images (b) and histology (c), d) and e)) for the healthy trachea after Zilver® Flex$^{TM}$ deployment. Re-epithelialization is visible around the stent struts (white region, blue arrow, sub-picture b)). The re-epithelialization as well as low inflammation and low thickening is revealed by means of the histology (sub-pictures c), d) and e)). **In the sub-figures c) and e) the stent struts are visible as black regions.**

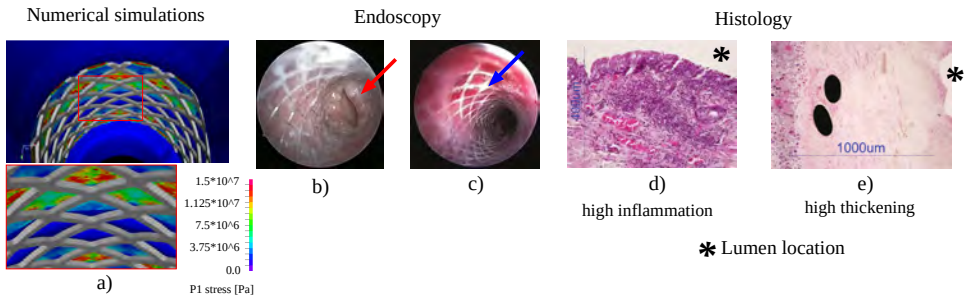


Figure 8. Comparison between numerical results (a), endoscopic images (b) and c)) and histology (d) and e)) for the healthy trachea after WallStent$^{TM}$ deployment. Numerical results provide high tensile stresses around stent struts at distal location (sub-picture (a)). The endoscopy shows the presence of granulomas at the distal section (indicated by the red arrow, sub-picture b)). Partial re-epithelialization is visible around the stent struts (blue arrow in sub-picture c)). The histology enhances tissue thickening and concentration of inflammatory cells such as neutrophils (sub-pictures d) and e)). **In the sub-figure e) the stent struts are visible as black regions.**